Acta Astronautica 127 (2016) 326–334

Contents lists available at ScienceDirect

Acta Astronautica

journal homepage: www.elsevier.com/locate/aa

Large eddy simulation of combustion characteristics in a kerosene fueled rocket-based combined-cycle engine combustor

Zhi-wei Huang, Guo-qiang He, Fei Qin *, Dong-gang Cao, Xiang-geng Wei, Lei Shi

Science and Technology on Combustion, Internal Flow and Thermal-structure Laboratory, Northwestern Polytechnical University, Xi'an Shaanxi 710072, PR China

ARTICLE INFO

Article history:
Received 6 November 2015
Received in revised form
2 June 2016
Accepted 3 June 2016
Available online 7 June 2016

Keywords:
Rocket-based combined-cycle
Large eddy simulation
Flame structure
Combustion characteristic
Flame stabilization mechanism

ABSTRACT

This study reports combustion characteristics of a rocket-based combined-cycle engine combustor operating at ramjet mode numerically. Compressible large eddy simulation with liquid kerosene sprayed and vaporized is used to study the intrinsic unsteadiness of combustion in such a propulsion system. Results for the pressure oscillation amplitude and frequency in the combustor as well as the wall pressure distribution along the flow-path, are validated using experimental data, and they show acceptable agreement. Coupled with reduced chemical kinetics of kerosene, results are compared with the simultaneously obtained Reynolds–Averaged Navier–Stokes results, and show significant differences. A flow field analysis is also carried out for further study of the turbulent flame structures. Mixture fraction is used to determine the most probable flame location in the combustor at stoichiometric condition. Spatial distributions of the Takeno flame index, scalar dissipation rate, and heat release rate reveal that different combustion modes, such as premixed and non-premixed modes, coexisted at different sections of the combustor. The RBCC combustor is divided into different regions characterized by their non-uniform features. Flame stabilization mechanism, i.e., flame propagation or fuel auto-ignition, and their relative importance, is also determined at different regions in the combustor.

1. Introduction

Rocket-based combined-cycle propulsion systems seamlessly combine the rocket engines with air-breathing engines. They can operate effectively at multiple modes in a wide range from takeoff, high altitude hypersonic cruise, and orbit [1,2]. The highly integrated design and excellent performance make them one of the most promising propulsion systems for future space transportation and near-space vehicles [3].

One of the study focuses on the development of such engines is the dual-mode (ramjet and scramjet modes) operation of a RBCC combustor, in which a thermally choked throat is achieved instead of a physical one [4]. Under the wide operating range and with variable inlet conditions, the primary rocket jet is highly coupled with the air inflow, and large vortex motion is formed. This further affects the vaporization, mixing, and combustion processes of secondary fuel injection by the fuel struts. These are considered as typical interactions between combustion and turbulence phenomena, in which the flow field in the combustor exhibits intrinsically unsteady characteristics [5,6]. The combustion process in the previous studies is assumed to be steady-state, ignoring the dynamic features [7–10]. Although Reynolds–Averaged Navier–Stokes or unsteady RANS simulations may satisfy the preliminary engineering designs, they showed significant limitations in high-efficiency combustion organization, flow-path optimization, and fuel injection control when considering various operating modes of a RBCC engine. Several studies concerning unsteady combustion processes have been carried out in the framework of large eddy simulation or RANS/LES hybrid methods on gas turbines [11,12], ramjets [13], scramjets [14–16], and dual-mode scramjets operate at ramjet mode [17]. Experiments on the dynamic combustion characteristics of scramjets [5,18,19] as well as combustion mode transition [20,21], have also been performed. However, rarely of them are direct relate to RBCC combustors. Although the application of LES to scramjet combustors has achieved certain success in recent years, a LES study that considers the unsteady combustion characteristics in a RBCC combustor is desirable. Our previous works have shown that the unsteady combustion characteristics in a RBCC combustor is significantly affected by the unsteady primary rocket jet [22,23], which is quite different from a scramjet combustor.

For a typical vehicle powered by RBCC, flight at Mach 3.0 (M_{flight}=3.0) is usually associated with ramjet mode. The robust

* Correspondence to: School of Astronautics, Northwestern Polytechnical University, Xi'an Shaanxi 710072, PR China.
E-mail address: qinfei@nwpu.edu.cn (F. Qin).

http://dx.doi.org/10.1016/j.actaastro.2016.06.016
0094-5765/

Nomenclature

Acronyms

RBCC	Rocket-Based Combined-Cycle
LES	Large Eddy Simulation
RANS	Reynolds–Averaged Navier–Stokes
FVM	Finite Volume Method
NSE	Navier-Stokes Equations
SGS	Sub-Grid Scale
FRC	Finite Rate Chemistry
NSCBC	Navier–Stokes Characteristic Boundary Condition
C–N	Crank–Nicolson
DES	Detached Eddy Simulation
FFT	Fast Fourier Transform

Variables

M_{flight}	flight Mach number (Dimensionless)
$M_{isolator}$	Mach number at the exit of the isolator (Dimensionless)
u_j	velocity in j direction (m/s)
p	pressure (Pa)
h	enthalpy (J/kg)
q	heat flux (W/m^2)
Y_m	mass fraction of species m (Dimensionless)
$V_{j,m}$	diffusion rate in j direction of species m (m/s)
ω_m	reaction rate of species m (kg/(s m^3))
τ_{ij}^{sgs}	sub-grid stress tensor (N/m^2)
h_j^{sgs}	sub-grid enthalpy flux (N/(m s))
$Y_{j,m}^{sgs}$	sub-grid convective flux of species m (W/m^3)
ν_t	sub-grid eddy viscosity coefficient (m^2/s)
Pr_t	turbulent Prandtl number (Dimensionless)
Sc_t	turbulent Schmidt number (Dimensionless)
E	activation energy (J/kmol)
A	pre-exponential factor (kmol/(cm^{3}s))
B	temperature exponent (Dimensionless)
T	temperature (K)
R	universal gas constant (J/(mol K))
k	reaction rate constant (Dimensionless)
Z	mixture fraction (Dimensionless)
G_{FO}	Takeno flame index (Dimensionless)
Y_O	mass fraction of oxidizer (Dimensionless)
Y_F	mass fraction of fuel (Dimensionless)
s	stoichiometric mass ratio (Dimensionless)
ν_O'	stoichiometric number of oxidizer (Dimensionless)
ν_F'	stoichiometric number of fuel (Dimensionless)
W_O	molecular weight of oxidizer (g/mol)
W_F	molecular weight of fuel (g/mol)
D	the mixture diffusion coefficient (kg/(m s))
HRR	heat release rate per unit volume (W/m^3)
HRR_{pre}	heat release by premixed combustion
HRR_{non}	heat release by non-premixed combustion
$HRR_{coe\text{-}pre}$	contribution coefficient of premixed combustion to the overall HRR
$HRR_{coe\text{-}non}$	contribution coefficient of non-premixed combustion to the overall HRR

Greek symbols

Δ	local grid size measurement (m)
ρ	density (kg/m^3)
ϕ	equivalence ratio (Dimensionless)
χ	scalar dissipation rate (Pa s/m^2)

Superscripts

$^\circ$	degree of angle
-	mass filtered quantities
~	Favre filtered quantities
sgs	the sub-grid scale quantities

and smooth operation of the combustor plays an important role in the fulfillment of certain space missions. Therefore, the typical operation point of a ground test direct-connect RBCC model engine operates at Mach 3.0 is examined in this study. A comprehensive study of the RBCC combustor dynamics that considers a facility inlet, an isolator, a primary rocket, two fuel struts, and two stage cavity flame-holders, is rarely found in open literatures yet. The present study attempts to improve the understandings of unsteady flow and flame dynamics for an experimental RBCC model combustor. Turbulent combustion is solved using a finite volume LES solver, based on the ANSYS Fluent software package [24].

2. Computational configuration and inflow conditions

The ground test direct-connect RBCC system includes two mainly sub-systems, the inflow simulating system and the model engine system. The inflow simulating system provides the necessary air inflow conditions at the inlet of the isolator in order to simulate the real flight state at the RBCC engine inlet. The test facility is capable of providing variable stagnation pressure and temperature conditions corresponding to flight Mach numbers of 2.5–6.0. In this study, the simulated flight Mach number is 3.0. This number is associated with the ramjet mode, which is also known as the cold start condition. The air inflow is preheated by an alcohol-fueled vitiation heater at a mass flow rate of 4.67 kg/s. Table 1 shows the simulated air inflow conditions.

Table 1
Flight conditions simulated by the ground test direct-connect experiment.

Altitude (km)	M_{flight}	Total pressure (MPa)	Total temperature (K)	Inflow rate (kg/s)	$M_{isolator}$
12	3.0	0.8	707	4.67	1.7

The model engine consists of a main strut, an isolator, a primary rocket, two fuel struts, two stage cavity flame-holders, and multi-stage rectangular combustors. The main strut acts as a Laval nozzle providing the required Mach number at the entrance of the isolator, which is a rectangular duct placed between the inlet and the combustor to reduce their interactions. The primary rocket is essentially a gas generator fueled by alcohol at 88.5 g/s and oxygen at 73.4 g/s. Therefore, the rocket jet is rich in fuel. It acts as an igniter and flame-holder for the combustion of secondary fuel. The nozzle for the exit jet is designed to be significantly over-expanded, in order to take the wide operating range of the RBCC into consideration. The three-stage combustors are made up of divergent channels with expansion angles of 2.0°, 1.5°, and 3.5°, and the lengths of 540 mm, 550 mm, and 460 mm, respectively. Two pairs of cavities are mounted oppositely one another in the first and second combustors to stabilize the flame of kerosene, which is injected by two fuel struts embedded in the first combustor

section at an equivalence ratio of 0.67. The entrance of the combustor is measured 140 mm in width and 50 mm in height, while the total length of the engine is 2100 mm. This model engine and its variations have long been studied in ground test experiments [22,23]. Fig. 1(a) and (b) shows a schematic of the simulated engine configuration and the detailed dimensions of the primary rocket, respectively.

Thirty-one pressure sensors flush-mounted to the wall are dispersed along the flow-path in ground tests, whose positions are indicated by the dots in Fig. 1(a). The acquisition frequency is set to 2000 Hz since the pressure oscillation showed obvious low-frequency feature. For a typical experiment, the air inflow system is firstly turned on 5.0 s before the pre-heater rocket's operation, heating the cold air to the desired temperature and pressure conditions of the simulated flight Mach number to a steady state. After more than 1.5 s, the fuel struts start to inject the liquid kerosene and more than 0.5 s later, the primary rocket is turned on to ignite the secondary fuel. The whole system operates at this state for more than 4.0 s to obtain a steady run. The pressure sensors start to record the pressure signals since the air inflow system is firstly started. The pressure data provides bases for LES model validation and combustion instability study, as well as for ground static thrust and specific impulse analysis [22,23].

3. Mathematical descriptions and numerical models

3.1. LES governing equations

Governing equations employed for LES of turbulent reactive flows are obtained using a local grid size delta Δ-based spatial filter to the Navier–Stokes equations for mass, momentum, energy, and species conservation laws [25]. After filtering, these equations can be expressed as,

$$\begin{cases} \dfrac{\partial \overline{\rho}}{\partial t} + \dfrac{\partial}{\partial x_j}\left(\overline{\rho}\tilde{u}_j\right) = 0 \\ \dfrac{\partial}{\partial t}\left(\overline{\rho}\tilde{u}_i\right) + \dfrac{\partial}{\partial x_j}\left(\overline{\rho}\tilde{u}_i\tilde{u}_j + \overline{p}\delta_{ij} - \tilde{\tau}_{ij} + \tau_{ij}^{sgs}\right) = 0 \\ \dfrac{\partial}{\partial t}\left(\overline{\rho}\tilde{h} - \overline{p}\right) + \dfrac{\partial}{\partial x_j}\left(\overline{\rho}\tilde{h}\tilde{u}_j + \tilde{q}_j - \tilde{u}_i\tilde{\tau}_{ij} + h_j^{sgs}\right) = 0 \\ \dfrac{\partial}{\partial t}\left(\overline{\rho}\tilde{Y}_m\right) + \dfrac{\partial}{\partial x_j}\left(\overline{\rho}\tilde{Y}_m\tilde{u}_j - \overline{\rho}\tilde{Y}_m\tilde{V}_{j,m} + Y_{j,m}^{sgs}\right) = \overline{\omega_m} \end{cases} \quad (1)$$

The subgrid-scale terms, $\tau_{ij}^{sgs}, h_j^{sgs}$ and $Y_{j,m}^{sgs}$, represent the subgrid stress tensor, enthalpy flux, and species convective flux, respectively, are expressed as,

$$\begin{cases} \tau_{ij}^{sgs} = -2\nu_t\tilde{S}_{ij} + \delta_{ij}\tau_{kk} \\ h_j^{sgs} = -\dfrac{\overline{\rho}\nu_t}{\mathrm{Pr}_t}\dfrac{\partial\tilde{h}}{\partial x_j} \\ Y_{j,m}^{sgs} = -\dfrac{\overline{\rho}\nu_t}{Sc_t}\dfrac{\partial\tilde{Y}_m}{\partial x_j} \end{cases} \quad (2)$$

3.2. Sub-grid flow and combustion models

The sub-grid flow model is used for the closure of eddy viscosity coefficient. The dynamic sub-grid scale kinetic energy model is used in this study [26]. It considers the transport of sub-grid turbulent energy and can handle the SGS turbulence adequately. The sub-grid combustion model is used to model the filtered reaction rates, ω_m, which are highly nonlinear functions of the local composition and temperature. The finite rate chemistry model, which can handle chemistry under various regimes including premixed and non-premixed combustion cases, is used to account for the interactions between the turbulence and chemistry in this

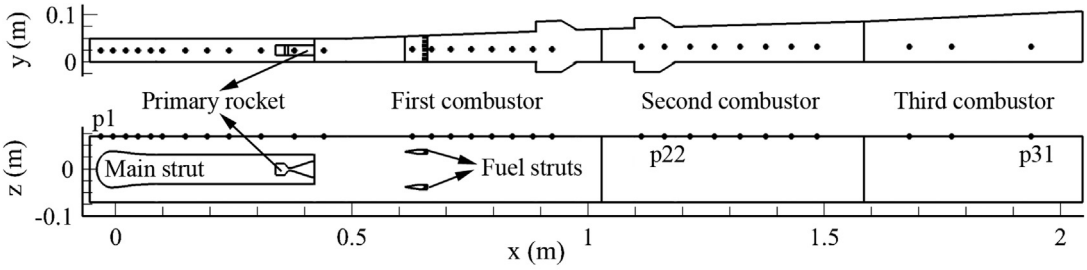

(a) Schematic of the model engine configuration.

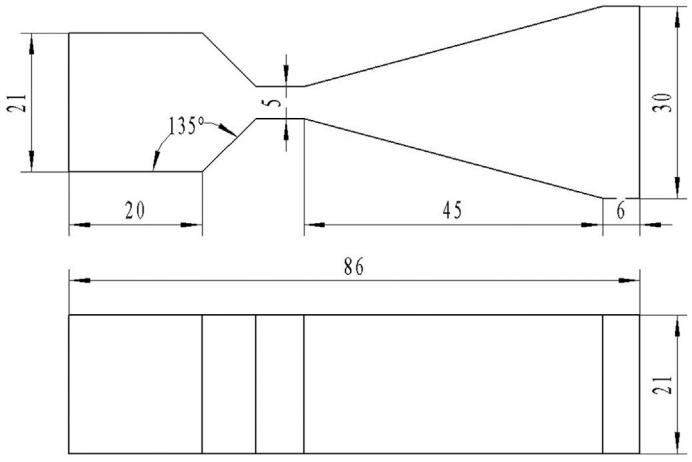

(b) The dimension of the primary rocket.

Fig. 1. Schematic of the RBCC model engine used for ground test experiments.

study [27].

3.3. Chemical kinetics and spray models for kerosene

Liquid kerosene (surrogated as $C_{10}H_{16}$) is used as the secondary fuel, which contains complex mixtures that are difficult to model using detailed chemistry models. In order to reduce the computational cost and time, a reduced kinetic mechanism of 3 reaction steps is adopted, for all parameters listed in Table 2 [28]. Eq. (3) gives the expression for the rate constants in the Arrhenius form. The reduced mechanism is not expected to predict reaction processes in detail, but at the very least, it should give reasonable macro effects of heat release on the combustion characteristics according to the previous experience [22].

$$k = AT^B \exp\left\{-E/(RT)\right\} \tag{3}$$

The spray field is assumed to be diluted and modeling of the liquid phase is the Lagrangian description [29]. The diluted spray approximation implies that when the particles interact with the gas phase, direct interaction between the drops is neglected. It precluded the inclusion of droplets breakdown and coalescence effects, which might be significant in a dense spray. The spray is divided into representative samples of discrete droplets whose motion and transport through the flow field are obtained using the Lagrangian formulas. Each of these "computational parcels" represent a group of particles with identical size, location, velocity and temperature. External forces on the droplets except inertia, drag and gravity are not considered. Governing equations for the particles' motion are given in [30].

For spray flames, the atomization characteristic of spray clusters plays a critical role in determining the combustion performance. Over-estimated or under-predicted droplet atomization rate would induce an erroneous delay of the gaseous combustion. The droplet break up model proposed in [31] is used to model the droplet atomization.

3.4. Boundary conditions and numerical methods

The mesh used for the simulation contains more than five million locally refined structural cells to ensure that grid resolution is in accordance with LES requirement. Coarser mesh containing more than 2.4 million cells used in the a prior study shows no significant difference in macro-parameters, such as pressure and temperature.

For the specification of boundary conditions, no-slip and adiabatic conditions are applied to all the walls, and typical y^+ values for the first grid points are of the order of 35. At the air inlet, the Navier–Stokes characteristic boundary condition is used to ensure a physical representation of the acoustic wave propagation, which should be non-reflective to prevent artificial forcing of acoustic fields into the computational domain. The Dirichlet boundary condition is applied at the primary rocket inlet, and all variables are extrapolated from the interior to avoid acoustic behavior uncertainties at the gas outlet boundary.

It is known that subsonic, transonic, and supersonic flows coexist in the RBCC combustor operating at ramjet mode at Mach 3.0. The multi-components such as the main strut, primary rocket, fuel struts, and cavity flame-holders in the model engine make the flow-path quite complex for the gas flows. In addition, using kerosene as a fuel involves atomization and evaporation models, which may also cause difficulties for the numerical simulation. In order to maintain numerical stability while properly capturing the unsteady features, second-order upwind schemes are used for the spatial discretization. A semi-implicit second-order Crank–Nicolson scheme is used for the temporal integration. The time step is close to 1 μs, basing on the maximum Courant numbers of no more than 0.5.

The computation is initialized by the air inflow conditions and commenced using a RANS model. Then it is changed to a detached eddy simulation when a reasonable cold field presents, and finally changed to a LES model. The computation is continued until the second-order statistical moments converged after about thirty flow-through times, equivalent approximately to 50 ms after the chemical reactions are turned on.

Table 2
Three-step reduced chemical kinetics for kerosene.

Step number	Reaction	A (cm^3/(mol s))	E (J/kg mol)	B
1	$C_{10}H_{16}+5O_2 \rightarrow 10CO+8H_2$	23,500	1.633×10^8	1
2	$2CO+O_2 \rightarrow 2CO_2$	3.48×10^8	8.42×10^7	2
3	$2H_2+O_2 \rightarrow 2H_2O$	3.0×10^{14}	0	−1

4. Results and discussion

4.1. Validation against experimental data

The LES solver is validated against experimental data by the pressure oscillation amplitude and frequency in the combustor as well as wall pressure distribution.

Table 3 shows the comparison of pressure oscillation amplitude and frequency at the same location in the combustor denoted as p22 in Fig. 1. The oscillation amplitude is measured using peak-to-peak values, while the frequency is obtained by applying a fast Fourier transform on the pressure signal. It is seen that both oscillation variables are well reproduced using LES.

Fig. 2 shows the pressure evolution with time measured by experiment and predicted by LES for intuitive views. The LES-predicted oscillation period is of the order of 6 ms, while the presented observation time is approximately 30 ms after the calculation converged. This is sufficient for the development of pressure to a dynamic steady state. However, as it is mentioned previously for the experimentally measured pressure the operating duration is several seconds and the sample rate is 2000 Hz, while the LES is performed in tens of milliseconds with a sample rate of about 1 MHz. Therefore, the time scales in Fig. 2(a) and (b) are different. The agreement of pressure oscillation amplitude proves that LES is a powerful tool for the study of flow and combustion phenomena in RBCC combustors.

Fig. 3 shows the wall pressure distribution of LES against experiment along the flow-path. The x-axis is non-dimensioned by the height of the combustor, while the y-axis is divided by the pressure value at the monitoring point, p6, the facility inlet. The short vertical lines outline the pressure oscillation amplitude at each point measured in the experiment. For most part of the flow-path except for the last four points in the second combustor and the three points in the third combustor, LES shows good agreement. Indeed, the high-altitude low back pressure condition is not modeled in ground tests. Therefore, the experimental back pressure is 1 atm, which is much higher than the back pressure used in

Table 3
LES validation of pressure oscillation characteristics at point p22.

Source	Oscillation peak-to-peak value	Oscillation frequency
Experiment	−7% to +8%	173.1 Hz
LES	−6% to +7%	164.6 Hz
Relative error (LES to experiment)	13.3%	4.9%

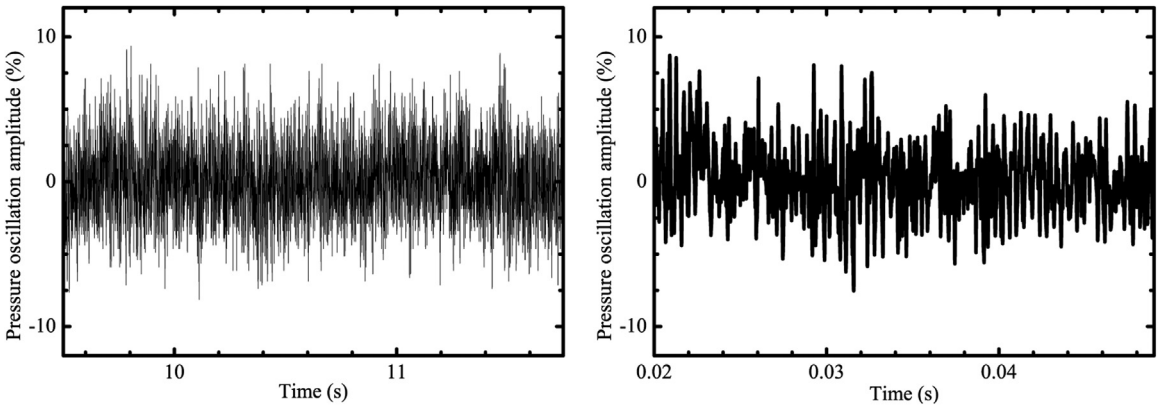

Fig. 2. Comparison of pressure oscillation amplitudes in the combustor.

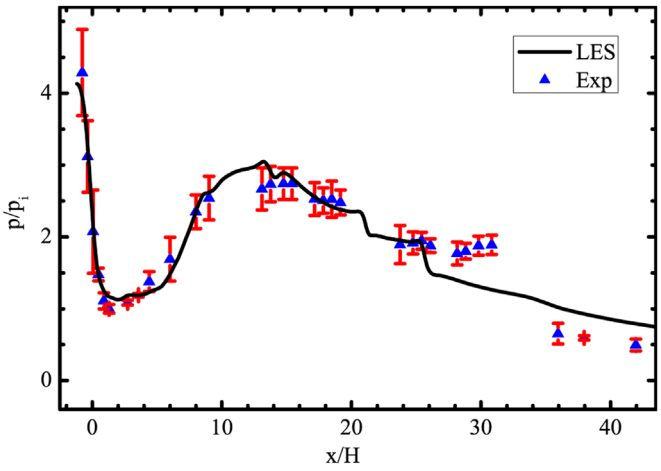

Fig. 3. LES pressure validation against experimental data.

the LES at the simulated flight altitude, 12 km. The pressure value at the point p6 in the experiment is about 1.5 atm. It can be seen that the three points in the third combustor are all lower than the back pressure, 1 atm. Conversely, the exit pressure in the LES is slightly higher than 1 atm, not to say that it is higher than the back pressure used in the simulation. Therefore, in the experiment the gas is over-expanded, whereas in the LES the gas is under-expanded. This might be the main reason for the large deviations at the last three points. It is also important to notice that step-like pressure variations are observed in LES at $x/H=20$ and 26. For the location of $x/H=20$, it is mainly due to the area contraction just after the first pair of cavities. Subsonic flow would expand and accelerate when the flow-path converges. Therefore, a sharp decrease is observed at $x/H=20$, just after the first pair of cavities. For $x/H=26$, which is shortly after the second pair of cavities, it is just the location of the thermal throat as it will be shown in Fig. 6. The gas flow here turned from subsonic to supersonic. Supersonic flow accelerates in a divergent channel, therefore, the pressure also shows a sharp decrease. But as the back pressure in the experiment is higher, the formation of thermal choking is shifted forward. Therefore, the pressure decrease at this location in the experiment is not as obvious as that in the LES.

4.2. Unsteady combustion characteristics

Unsteady combustion characteristics are highlighted by the comparison with the RANS results. Fig. 4 shows the instantaneous (48 ms) temperature by LES and the one time-averaged from RANS calculation at two different heights of the combustor, $y/H=0.50$ and 0.75, respectively. It may be noted that high-temperature zones exist mainly in two regions. These regions are the boundary shear layers formed between the primary rocket jet and the incoming air, and the extensive areas following the fuel struts. Large gradients of velocity and temperature exist between the rocket jet and the air inflow, and turbulent mixing/reacting shear layers are formed. The fuel-rich rocket jet mixes and burns in the presence of fresh air, releasing a large amount of heat. Flame scales out transversely and longitudinally upwards. The secondary combustion of the rocket jet is powerful enough to reach the fuel struts, where the injected liquid kerosene is successfully ignited and a continuous flame sustains after the struts.

The temperature shows significant unsteady characteristics when comparing Fig. 4(a) with Fig. 4(b). It is found that the primary rocket jet oscillates and is distorted, and the shear layers formed are quite irregular. The flame after the fuel struts is also distorted and wrinkled because of the shedding of vortices and the instabilities of the shear layers. These unsteady processes are well captured using LES, while the RANS calculation yields a rather smooth temperature distribution. The highest temperature zones last to the end of the first combustor steadily in RANS, which is significantly different from that of the instantaneous result in LES. Under the combined effects of the occurrence of thermal throat (shown in Fig. 6), the eddy dissipation (shown in Fig. 8), and the combustion heat release (shown in Fig. 10), the flow shows remarkable homogenization features after the second pair of cavities. After this point, large-scale vortex structures no longer exists. The results of the LES and RANS methods show no significant difference thereafter.

Fig. 5 shows the instantaneous and time-averaged mass fraction of CO_2 at the same site as the one shown in Fig. 4. CO is one of the major components of the rocket jet, and CO_2 is the combustion product. A similar tendency to that of the temperature in Fig. 4 is observed here. Therefore, from Fig. 4 and Fig. 5 it may be concluded that the main heat release region in the combustor shows obvious unsteady characteristics, where the flame surface and the large-scale vortex structures are visibly distorted. The spatial distribution of kerosene heat release is largely affected, and the LES results shows some differences when compared with the RANS results.

It is mentioned that the thermal choking plays an important role in homogenizing the flow field after the second pair of cavities. Fig. 6 shows the contour of Mach number at the center plane of the combustor and other six transversal sections. The instantaneous structure of the thermal throat is depicted by the iso-

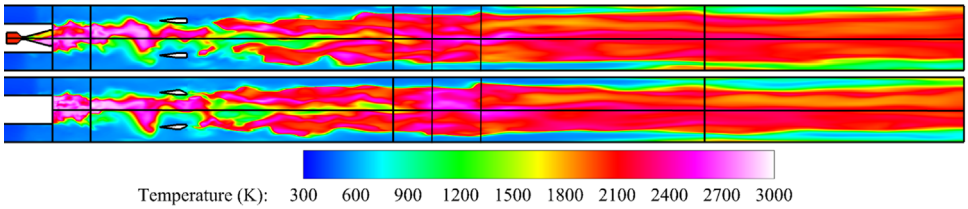

(a) Instantaneous temperature at different heights by LES: y/H = 0.50 (upper) and y/H = 0.75 (lower).

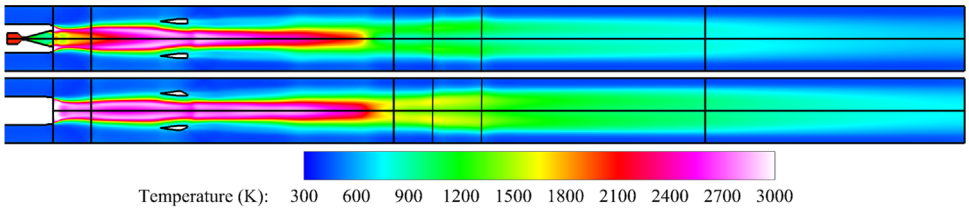

(b) Time-averaged temperature at different heights by RANS: y/H = 0.50 (upper) and y/H = 0.75 (lower).

Fig. 4. Comparison of temperature fields for LES and RANS.

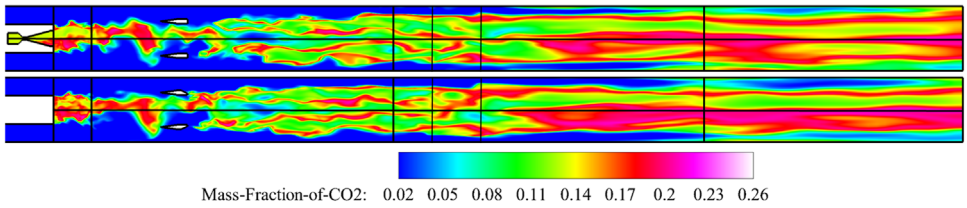

(a) Instantaneous mass fraction of CO_2 at different heights by LES: y/H = 0.50 (upper) and y/H = 0.75 (lower).

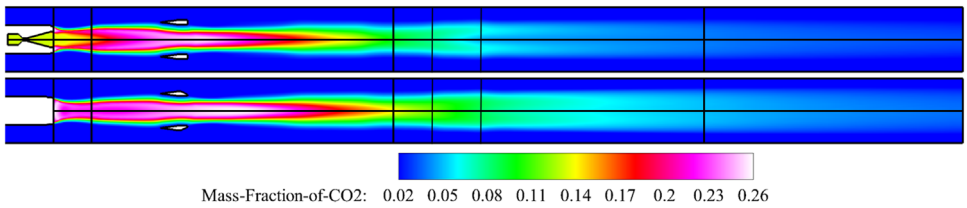

(b) Time-averaged mass fraction of CO_2 at different heights by RANS: y/H = 0.50 (upper) and y/H = 0.75 (lower).

Fig. 5. Comparison of mass fractions of CO_2 for LES and RANS.

contour of Ma = 1. Basically, three zones isolated by pre-combustion shocks in the isolator and thermal throat after the second pair of cavities with distinct characteristics are identified. The first is from the engine inlet to the front of pre-combustion shocks, where no chemical reaction takes place but flow with supersonic velocity. The second starts from the end of the shock trains to the front of thermal throat, where fierce combustion takes place mainly in subsonic speed. The third one is after the thermal throat, where moderate reaction takes place in the supersonic flow of the hot combustion product. To see the structure of the thermal throat clearly, it is locally enlarged after the second cavities at the right corner of the image. The black arrows denotes the flow direction, which is oppose to that shown in its left. Thermal choking occurs just after the second pair of cavities. Therefore, temperature is homogenized by thermal choking at this position.

4.3. *Turbulent flame structures*

In this section, flame structures and combustion modes for the RBCC combustor are studied using three parameters. The first is the mixture fraction, denoted by Z [32]:

$$Z = \left(\phi \cdot Y_F/Y_F^0 - Y_O/Y_O^0 + 1\right)/(\phi + 1) \tag{4}$$

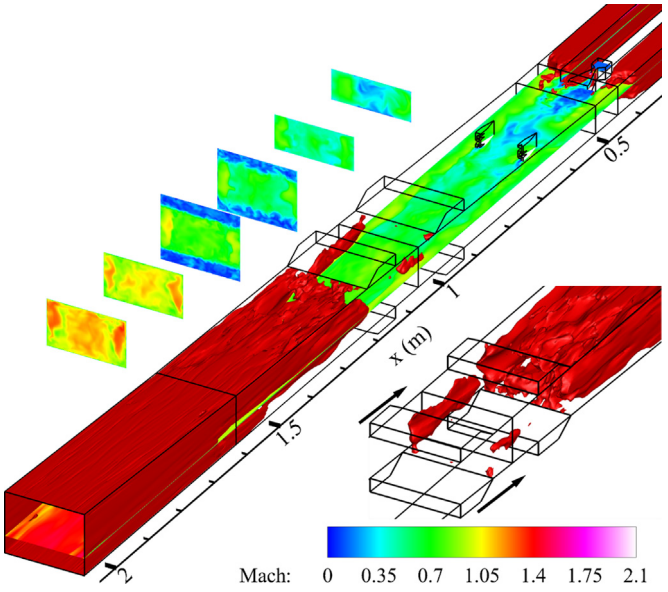

Fig. 6. Contour of Mach number and the instantaneous structure of the thermal throat.

The ϕ is an important chemical parameter in diffusion flames corresponding to the ratio obtained when premixing the same mass quantities of fuel and oxidizer. Z is a passive scalar and changes because of diffusion and convection, but not change due to reaction. Moreover, it represents the most likely flame surfaces at stoichiometric value [32].

The second is the Takeno flame index, denoted by G_{FO} [33]:

$$G_{FO} = (\nabla Y_F \cdot \nabla Y_O)/(|\nabla Y_F| \cdot |\nabla Y_O|) \tag{5}$$

This parameter identifies different modes for premixed or non-premixed combustion.

The third is the scalar dissipation rate, denoted by χ [34]:

$$\chi = 2D\left[\left(\frac{\partial Z}{\partial x}\right)^2 + \left(\frac{\partial Z}{\partial y}\right)^2 + \left(\frac{\partial Z}{\partial z}\right)^2\right] \tag{6}$$

which is essentially the rate of mixing between the fuel and oxidizer.

Fig. 7 shows the contour surfaces of stoichiometric mixture fraction rendered by temperature to represent the flame location after the fuel struts. Highly wrinkled large flame structures are observed after the fuel struts, in the two pairs of cavities and further downstream. The motions of unsteady turbulent vortices effectively increase the area of combustion and the speed of turbulent flame. Flame after the second pair of cavities is smoother than the flame upstream and shows a noticeable ribbon-like distribution feature. It is important to note that flame is sustained after each fuel strut, although expansion towards the central flow is limited. Furthermore, the two flame ribbons after the fuel struts show inconsistencies with one another at the same instant. This is an important indicator of the unsteady combustion characteristics, especially when their operating conditions are identical.

The temperature profile in Fig. 7 also shows significant variation with distance from where the kerosene is injected. In the near-strut region, the cold liquid kerosene absorbs a large amount of heat for its evaporation and fierce combustion afterwards. Due to the high temperature rocket jet, combustion is not suspended but sustained. After a short distance, the vaporized gaseous kerosene is successfully ignited and the flame temperature increases as the flow going downwards until it reaches the second pair of cavities. After this point, a thermally choked "nozzle" is formed due to the combined effects of heat release and the variation in flow-path area. The temperature profile almost achieved equilibrium. The heat release from combustion is balanced by the loss due to the expansion of supersonic flow in a divergent channel, and the flame appears to keep at a constant temperature.

Fig. 8 shows contour of scalar dissipation rate at different cross-sections and in the center plane of the primary rocket. It is found that intense mixing takes place mainly in two regions: the outer boundary of the mixing/reacting shear layers formed between the rocket jet and the air inflow, and the extensive region following the fuel struts. Due to the large velocity and temperature gradients between the rocket jet and the air inflow, strong shear force and intense convection between the different streams, intense mixing is produced. For the regions after the fuel struts, high concentration of gaseous kerosene and its successful ignition, as well as large velocity gradient exists within the low-speed recirculation zone at the trailing edge of the struts. All of these conditions result in intense species, energy, and momentum transport. The χ-value shows a decreasing tendency along the flow-path as a whole, owing to energy cascade transport and eddy dissipation.

Fig. 9 shows the normalized flame index after the primary rocket to identify different combustion modes in the combustor. It

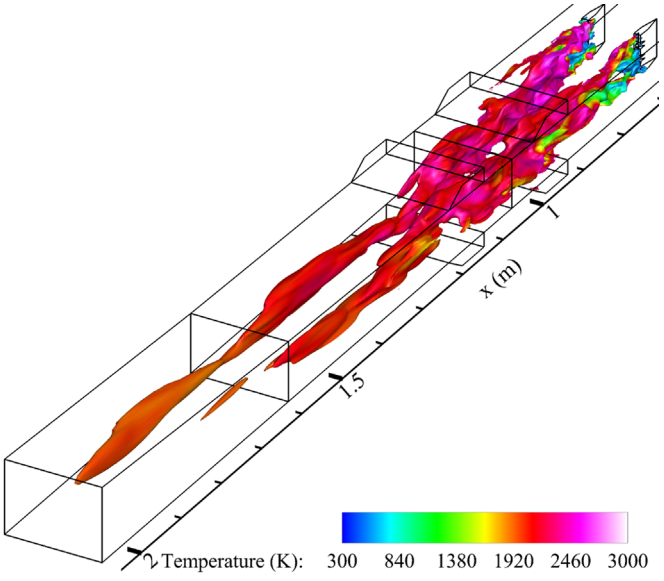

Fig. 7. Iso-surface of stoichiometric mixture fraction colored by temperature after the fuel struts.

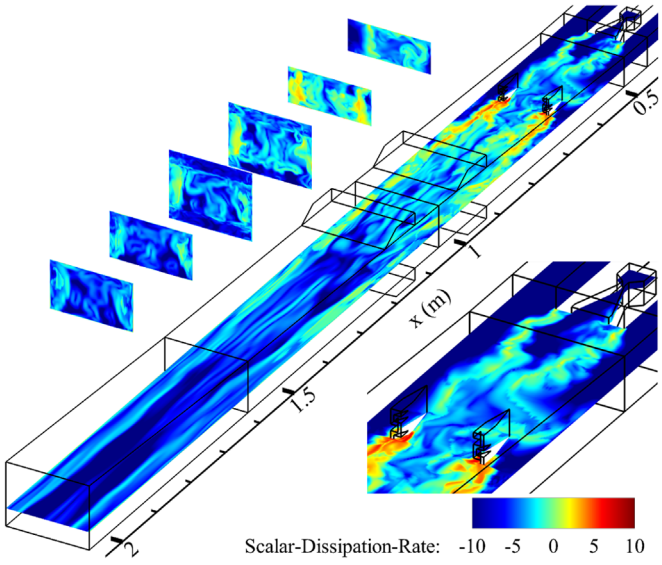

Fig. 8. Scalar dissipation rate distribution in the combustor (logarithmic scale).

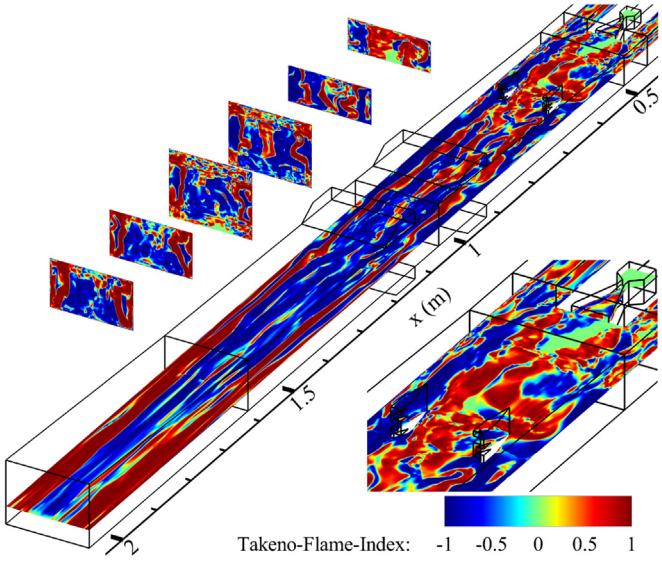

Fig. 9. Takeno flame index distribution.

assumes that gradients in the fuel and oxidizer are aligned for premixed flame, and anti-aligned for non-premixed flame [33]. Essentially, three different regions are identified. The first is the region of shear layers formed between the rocket jet and the air inflow, as well as all the near-wall regions, which burns mainly in premixed mode. The second is the core region of the rocket jet, where no combustion takes place. The third is the central region of the combustor after the first pair of cavities, which burns mainly in non-premixed mode. Formation of the combustion mode in each region may be explained in this way. For the region just after the rocket, as the high temperature rocket jet is a mixture of fuel-rich combustible gas, it firstly mixes and diffuses to the air inflow to get away from the fuel-rich extinction limit. Therefore, just inside the rocket jet shear layer there is no combustion or in a quite weak diffusion combustion mode. However, due to the strong reactivity of the rocket jet, once the equivalence ratio is proper for combustion to take place, the high temperature jet flame propagates to the shear layer and premixed flame front is formed. In the region after the first cavities where non-premixed combustion dominates, the combustion of kerosene and its decomposition products is in dominate while the reaction of the rocket jet is almost complete. Temperature of the injected kerosene is much lower compared with the upstream exhaust gas, and its atomization and evaporation also absorbs a large amount of heat energy. The overall combustion is limited by the decomposition of kerosene and the diffusion rates to the surroundings. Therefore, non-premixed combustion mode is seen dominate in this region.

The concept of flame index is helpful to study the combustion modes. However, it is not a chemical property of the mixture. It measures the scalar gradient alignments regardless of the reaction progress, which may also peak in non-reactive cases, such as for premixed or non-premixed opposed jets at room temperature. In these cases, the magnitude of the flame index may be large solely due to high-flow strain and mixing rates. Therefore, a flame may or may not actually exists where the flame index peaks. An additional reaction variable is required to delineate different combustion modes. The spatial distribution of heat release rate is chosen for assistant analysis [35]. Fig. 10 shows the power of reaction per unit volume in the combustor. The regions where combustion actually takes place with distinct heat release are remarkably narrower than those shown in Fig. 9. It means that the regions where heat release is nonzero the flame index must be nonzero, but not vice versa. The largest heat release occurs in the downstream regions along the fuel struts. In the center flow region after the second pair of cavities, reactions are limited in intensity. It may be concluded from Figs. 9 and 10 that the auto-ignition flames in the regions along the fuel struts precedes the premixed flames in the central flow region, where flame propagation is the dominate flame stabilization mechanism.

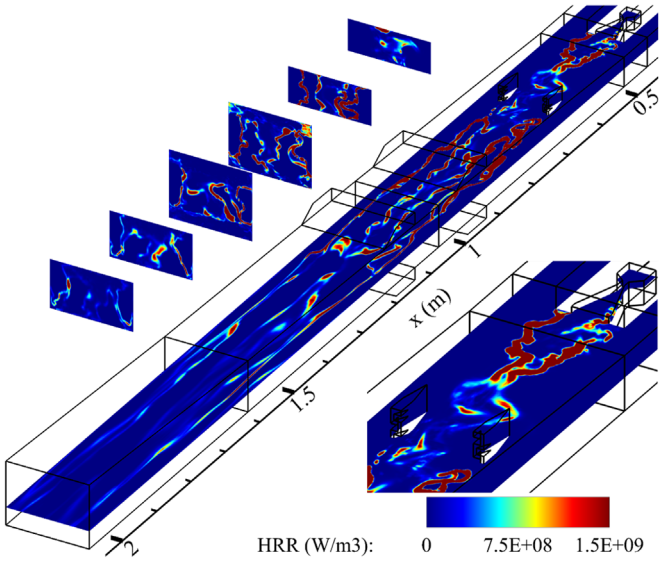

Fig. 10. Heat release rate per unit cell volume.

To further study the importance of premixed and non-premixed combustion heat release quantitatively, two variables are defined:

$$\begin{cases} HRR_{pre} = (G_{FO} + |G_{FO}|)/2G_{FO} \times HRR \\ HRR_{non} = (G_{FO} - |G_{FO}|)/2G_{FO} \times HRR \end{cases} \quad (7)$$

It is obvious that for premixed combustion $HRR_{pre}=HRR$ while $HRR_{non}=0$, for non-premixed combustion $HRR_{pre}=0$ while $HRR_{non}=HRR$. Therefore, heat release by different combustion modes is distinguished. In this definition, it also excludes the situation where G_{FO} is nonzero while HRR is zero. It means that only the region where combustion actually takes place is taken into consideration. HRR_{pre} and HRR_{non} are integrated on each cell volume to obtain the contribution coefficient, HRR_{coe}, to the overall HRR. It is found that $HRR_{coe\text{-}pre}=62\%$ while $HRR_{coe\text{-}non}=38\%$. Although premixed combustion is narrow in space, it is important for the overall heat release. The heat release different combustion modes contribute to and the distribution pattern can be used for passive control of fuel injection schemes and combustion organization manners, which is widely used for mode transition in dual-mode scramjets [5,36] and RBCC engines [37].

5. Conclusions

This study reports the combustion characteristics of a RBCC engine combustor operating at ramjet mode numerically. LES with sprayed and vaporized kerosene is used to study the intrinsically unsteady features of combustion in such a propulsion system. Validation of pressure oscillation amplitude and frequency in the combustor as well as the wall pressure distribution indicates the applicability of the current LES solver. The unsteady characteristics captured by LES are highlighted by comparison with a RANS calculation. Turbulent flame structures are also studied. Stoichiometric mixture fraction is used to indicate the flame location, which shows a ribbon-like distribution pattern. Mixing characteristics are analyzed using the scalar dissipation rate. Two intense mixing zones are recognized, one is in the shear layer of the primary rocket jet and the other is after the fuel struts. Combination study of the Takeno flame index and heat release rate spatial distribution indicates that different combustion modes and flame stabilization mechanisms exist in different regions of the combustor. The first is the shear layer of the rocket jet, where combustion takes place mainly in premixed mode, and flame propagation is the dominate stabilization mechanism. The second is the core region of the rocket jet, where almost no reaction takes place. The third is the extensive zone after the fuel struts, where non-premixed combustion takes place and auto-ignition is mainly responsible for the flame stabilization.

Conflict of interest

The authors declare that they have no conflict of interest.

Acknowledgments

This work was financially supported by the National Natural

Science Foundation of China (Contract no. 91541110) and the Fundamental Research Funds for the Central Universities (Contract no. 3102015ZY006).

References

[1] K.W. Flaherty, K.M. Andrews, G.W. Liston, Operability benefits of airbreathing hypersonic propulsion for flexible access to space, J. Spacecr. Rocket. 47 (2) (2010) 280–287.

[2] A.P. Kothari, J.W. Livingston, C. Tarpley, V. Raghavan, K.G. Bowcutt, T.R. Smith, Rocket Based Combined Cycle Hypersonic Vehicle Design for Orbital Access, AIAA Paper 2011-2338, 2011.

[3] M. Kodera, H. Ogawa, S. Tomioka, S. Ueda, Multi-objective Design And Trajectory Optimization Of Space Transport Systems with RBCC Propulsion Via Evolutionary Algorithms and Pseudo-spectral Methods, AIAA Paper 2014-0629, 2014.

[4] J. Lee, T.M. Krivanek, Design and Fabrication of the ISTAR Direct-connect Combustor Experiment at the NASA Hypersonic Tunnel Facility, AIAA Paper 2005-0611, 2005.

[5] D.J. Micka, J.F. Driscoll, Combustion characteristics of a dual-mode scramjet combustor with cavity flameholder, Proc. Combust. Inst. 32 (2) (2009) 2397–2404.

[6] A. Roux, L.Y.M. Gicquel, S. Reichstadt, N. Bertier, G. Staffelbach, F. Vuillot, T. J. Poinsot, Analysis of unsteady reacting flows and impact of chemistry description in large eddy simulations of side-dump ramjet combustors, Combust. Flame 157 (1) (2010) 176–191.

[7] M. Emory, V. Terrapon, R. Pečnik, G. Iaccarino, Characterizing the Operability Limits of the HyShot II Scramjet Through RANS Simulations, AIAA Paper 2011-2282, 2011.

[8] Y. You, H. Luedeke, K. Hannemann, Injection and mixing in a scramjet combustor: DES and RANS studies, Proc. Combust. Inst. 34 (2) (2013) 2083–2092.

[9] K. Makowka, T. Sattelmayer, N.C. Dröske, J.J. Vellaramkalayil, J.V. Wolfersdorf, Unsteady RANS Investigation of a Hydrogen-fueled Staged Supersonic Combustor With Lobed Injectors, AIAA Paper 2014-3215, 2014.

[10] M.B. Solmaz, S. Uslu, O. Uzol, Unsteady RANS for Simulation of High Swirling Non-premixed Methane-air Flame, AIAA Paper 2014-3473, 2014.

[11] Y.C. See, M. Ihme, LES Investigation of Flow Field Sensitivity in a Gas Turbine Model Combustor, AIAA Paper 2014-0621, 2014.

[12] G. Bulat, E. Fedina, C. Fureby, W. Meier, U. Stopper, Reacting flow in an industrial gas turbine combustor: LES and experimental analysis, Proc. Combust. Inst. 35 (3) (2015) 3175–3183.

[13] L.Y.M. Gicquel, A. Roux, LES to ease understanding of complex unsteady combustion features of ramjet burners, Flow Turbul. Combust. 87 (2) (2011) 449–472.

[14] J.Y. Choi, F.H. Ma, V. Yang, Dynamics Combustion Characteristics in Scramjet Combustors With Transverse Fuel Injection, AIAA Paper 2005-4428, 2005.

[15] H. Koo, P. Donde, V. Raman, LES-based Eulerian PDF approach for the simulation of scramjet combustors, Proc. Combust. Inst. 34 (2) (2013) 2093–2100.

[16] H.B. Wang, Z.G. Wang, M.B. Sun, N. Qin, Large eddy simulation of a hydrogen-fueled scramjet combustor with dual cavity, Acta Astronaut. 108 (2015) 119–128.

[17] J. Li, F.H. Ma, V. Yang, K.C. Lin, T.A. Jackson, A Comprehensive Study of Combustion Oscillations in a Hydrocarbon-fueled Scramjet Engine, AIAA Paper 2007-836, 2007.

[18] K.C. Lin, K. Jackson, R. Behadadnia, T.A. Jackson, F.H. Ma, V. Yang, Acoustic characterization of an ethylene-fueled scramjet combustor with a cavity flameholder, J. Propul. Power 26 (6) (2010) 1161–1169.

[19] C. Zhang, Q.C. Yang, J.T. Chang, J.F. Tang, W. Bao, Nonlinear characteristics and detection of combustion modes for a hydrocarbon fueled scramjet, Acta Astronaut. 110 (2015) 89–98.

[20] T. Kouchi, G. Masuya, T. Mitani, S. Tomioka, Mechanism and control of combustion-mode transition in a scramjet engine, J. Propul. Power 28 (1) (2012) 106–112.

[21] Y. Zhang, B. Chen, G. Liu, B.X. Wei, X. Xu, Influencing factors on the mode transition in a dual-mode scramjet, Acta Astronaut. 103 (2014) 1–15.

[22] Z.W. Huang, G.Q. He, F. Qin, X.G. Wei, D.G. Cao, Large Eddy Simulation of Effects of Primary Rocket Jet on Low Frequency Combustion Instability in a RBCC Combustor, AIAA Paper 2015-3623, 2015.

[23] Z.W. Huang, G.Q. He, F. Qin, X.G. Wei, L. Shi, Supersonic turbulent combustion characteristics of a rocket-based combined-cycle engine combustor, in: Proceedings of 10th ASPACC, 2015.

[24] Fluent Inc., ANSYS, Inc., ANSYS FLUENT 13.0 Theory Guide, 2010.

[25] P. Moin, K. Squires, W. Cabot, S. Lee, A dynamic subgird-scale model for compressible turbulence and scalar transport, Phys. Fluids 3 (11) (1991) 2746–2757.

[26] W.W. Kim, S. Menon, Application of the Localized Dynamic Subgrid-scale Model to Turbulent Wall-bounded Flows, AIAA Paper 1997-0210, 1997.

[27] V. Parisi, E. Giacomazzi, C. Bruno, Analysis of Small Scale Turbulence-combustion Interaction for LES Modeling, AIAA Paper 2005-1283, 2005.

[28] T.S. Wang, Thermophysics characterization of kerosene combustion, J. Thermophys. Heat Transf. 15 (2) (2001) 140–147.

[29] F. Genin, S. Menon, LES of Supersonic Combustion of Hydrocarbon Spray in a Scramjet, AIAA Paper 2004-4132, 2004.

[30] G. Tomar, D. Fuster, S. Zaleski, S. Popinet, Multiscale simulations of primary atomization, Comput Fluids 39 (10) (2010) 1864–1874.

[31] F.X. Tanner, Liquid jet atomization and droplet breakup modeling of non-evaporating diesel fuel sprays, SAE Trans 106 (3) (1997) 127–140.

[32] T.J. Poinsot, D. Veynante, Theoretical and Numerical Combustion, third ed., Edwards, Philadelphia, 2012.

[33] H. Yamashita, M. Shimada, T. Takeno, A numerical study on flame stability at the transition point of jet diffusion flames, in: Proceedings of Symposium (International) on Combustion, 26 (1), 1996, pp. 27–34.

[34] E.R. Hawkes, R. Sankaran, J.C. Sutherland, J.H. Chen, Direct numerical simulation of turbulent combustion: fundamental insights towards predictive models, J. Phys. 16 (1) (2005) 65–79.

[35] Z.Y. Luo, C.S. Yoo, E.S. Richardson, J.H. Chen, C.K. Law, T.F. Lu, Chemical explosive mode analysis for a turbulent lifted ethylene jet flame in highly-heated coflow, Combust. Flame 159 (1) (2012) 265–274.

[36] R.F. Cao, J.T. Chang, W. Bao, M.L. Guo, J. Qin, D.R. Yu, Z.Q. Wang, Analysis of combustion mode and operating route for hydrogen fueled scramjet engine, Int. J. Hydrogen Energy 38 (14) (2013) 5928–5935.

[37] M. Kodera, S. Ueda, Numerical Analysis of Transient Phenomena to Ramjet Mode in a RBCC Combustor, AIAA Paper 2015-3591, 2015.